

Electromagnetic field evolution in relativistic heavy-ion collisions

V. Voronyuk

*Joint Institute for Nuclear Research, Dubna, Russia
 Frankfurt Institute for Advanced Study, Frankfurt, Germany and
 Bogolyubov Institute for Theoretical Physics, Kiev, Ukraine*

V. D. Toneev

*Joint Institute for Nuclear Research, Dubna, Russia and
 Frankfurt Institute for Advanced Study, Frankfurt, Germany*

W. Cassing

Institute for Theoretical Physics, University of Giessen, Giessen, Germany

E. L. Bratkovskaya

*Institute for Theoretical Physics, University of Frankfurt, Frankfurt, Germany and
 Frankfurt Institute for Advanced Study, Frankfurt, Germany*

V. P. Konchakovski

*Institute for Theoretical Physics, University of Giessen, Giessen, Germany and
 Bogolyubov Institute for Theoretical Physics, Kiev, Ukraine*

S. A. Voloshin

Wayne State University, Detroit, Michigan, USA

The hadron string dynamics (HSD) model is generalized to include the creation and evolution of retarded electromagnetic fields as well as the influence of the magnetic and electric fields on the quasiparticle propagation. The time-space structure of the fields is analyzed in detail for non-central Au+Au collisions at $\sqrt{s_{NN}} = 200$ GeV. It is shown that the created magnetic field is highly inhomogeneous but in the central region of the overlapping nuclei it changes relatively weakly in the transverse direction. For the impact parameter $b = 10$ fm the maximal magnetic field - perpendicularly to the reaction plane - is obtained of order $eB_y/m_\pi^2 \sim 5$ for a very short time ~ 0.2 fm/c, which roughly corresponds to the time of a maximal overlap of the colliding nuclei. We find that at any time the location of the maximum in the eB_y distribution correlates with that of the energy density of the created particles. In contrast, the electric field distribution, being also highly inhomogeneous, has a minimum in the center of the overlap region. Furthermore, the field characteristics are presented as a function of the collision energy and the centrality of the collisions. To explore the effect of the back-reaction of the fields on hadronic observables a comparison of HSD results with and without fields is exemplified. Our actual calculations show no noticeable influence of the electromagnetic fields - created in heavy-ion collisions - on the effect of the electric charge separation with respect to the reaction plane.

PACS numbers: 25.75.-q, 25.75.Ag

I. INTRODUCTION

The study of the properties of QCD matter in the presence of strong uniform magnetic fields has attracted much attention during recent years due to several remarkable observations. They include such a universal phenomenon as the magnetic catalysis [1–3] in which the magnetic field acts as a strong catalyst of dynamical flavor symmetry breaking which might lead to the generation of a dynamical fermion mass. Furthermore, in dense QCD matter in the presence of an external magnetic field and/or topological defects, a spontaneous creation of axial currents [4] may happen. Moreover, at finite baryon density, due to a response of the QCD ground state to a strong magnetic field, a metastable object, the π^0 domain wall

(or “Goldstone current state” in quark matter), could appear which energetically may be more favorable than nuclear matter at the same density [5]. The presence of a magnetic field also favors the formation of spatially inhomogeneous spiral-like quark condensate configurations at low temperatures and non-zero chemical potentials [6]. The influence of a constant magnetic field on possible color-superconducting phases (the color Meissner effect) has also actively been discussed [7]. A clarification of such phenomena by experimental observations requires e.g. the production of QCD matter in relativistic heavy-ion collisions where in non-central reactions strong electromagnetic fields are created by the charged four-current of the spectators.

In this general respect exact solutions of the quantum field equations of motion are of special interest. The lat-

ter supply us with microscopic insight for problems of relativistic charged particle motion in electromagnetic fields of terrestrial experimental devices as well as in astrophysics and cosmology. In particular, they apply to the development of the quantum theory of synchrotron radiation [8] and also for the description of interacting particles, including electrons and neutrinos, especially in matter in the presence of external electromagnetic fields [9].

More specifically, the quark-hadron and chiral symmetry restoration transitions might be dramatically modified in the presence of a strong magnetic field. We recall that without a magnetic field a crossover at $T = T_c \approx 160$ MeV is realized at vanishing baryon chemical potential μ_q . The presence of a strong magnetic background turns this picture within a linear sigma model into a weak first order phase transition [10, 11] whereas in the Nasmbu-Jona-Lasinio NJL model the crossover remains [12, 13]. This contradiction is reconciled by noting a crucial role of the vacuum contribution from quarks. The vacuum contribution seems to soften the order of phase transition: the first order phase transition - which would be realized in the absence of the vacuum contribution - becomes a smooth crossover if the system with vacuum quark loops included [14].

Within the Polyakov-Nambu-Jona-Lasinio (PNJL model) it was shown that the external field acts as a catalyst for dynamical symmetry breaking which increases the critical temperature with increasing strength of the magnetic field and sharpens the transition [15] in agreement with lattice QCD calculations [16]. Very recently, an astonishing feature has been demonstrated in effective models in that lines of the finite temperature deconfinement and chiral transitions can split in a strong magnetic background [14, 17]. We also mention that the presence of a strong constant magnetic field modified also the nature of the electroweak phase transition in the evolution of the universe at its early stages [18].

In the last few years, particular attention has been paid to the chiral magnetic effect (CME) closely related to a possible local \mathcal{P} and \mathcal{CP} symmetry violation in strong interactions as suggested in Ref [19] and widely discussed in Refs. [15, 20–23]. This effect originates from the existence of nontrivial topological configurations of gauge fields and their interplay with the chiral anomaly which results in an asymmetry between left- and right-handed quarks. Such a chiral asymmetry, when coupled to a strong magnetic field as created by colliding nuclei perpendicularly to the reaction plane, induces an electric charge current along the direction of a magnetic field thereby separating particles of opposite charges with respect to the reaction plane. Thus, such topological effects in QCD might be observed in heavy-ion collisions directly in the presence of very intense external electromagnetic fields due to the “Chiral Magnetic Effect” as a manifestation of the spontaneous violation of the \mathcal{CP} symmetry. Recently, topological charge fluctuations and possible CME have been confirmed by QCD lattice calculations in quenched $SU(2)$ gauge theory [24] and in

QCD+QED with dynamical $2 + 1$ quark flavors [25].

One should note that in contrast to all the cases mentioned above, the magnetic field in the CME is not constant and acts only during a very short time. The maximal strength of the electromagnetic field eB_y created in relativistic heavy-ion collisions is very high $eB_y \sim 5 m_\pi^2$ but its duration is $t \sim 0.2$ fm/c for Au+Au at $\sqrt{s_{NN}} = 200$ GeV collisions and impact parameter $b = 10$ fm, as was estimated dynamically in [21, 26, 27].

It is remarkable that the proposed CME observable, i.e. the electric charge asymmetry of produced particles with respect to the reaction plane, has been recently measured by the STAR Collaboration [28, 29]. Qualitatively the experimental results agree with the magnitude and gross features of the theoretical predictions for local \mathcal{P} -odd violation in heavy-ion collisions. The observed signal can not be described by the background models used in [28, 29], however, alternative mechanisms resulting in a similar charge separation effect are not fully excluded (see e.g. Refs. [30–35]). This issue is under intensive debate now.

The aim of this paper is to study the space-time evolution of (electro-)magnetic fields formed in relativistic heavy-ion collisions. The Hadron String Dynamics (HSD) transport code [36] is used as a basis of our considerations. In contrast with the UrQMD model without including electromagnetic fields (previously used for the analysis [28, 29]), the HSD model corresponds to Kadanoff-Baym rather than Boltzman kinetic equations and treats the nuclear collisions in terms of quasiparticles with a finite width. In our approach the dynamical formation of the electromagnetic field, its evolution during a collision and influence on the quasiparticle dynamics as well as the interplay of the created magnetic and electric fields and back-reaction effects are included simultaneously.

The article is organized as follows: In Sect. II the model is presented and it is shown how the formation of the electromagnetic field and particle propagation in this background can be implemented in the HSD transport code. In Sect. III the space-time structure of the formed electromagnetic fields, their correlations with the energy density of produced particles, the correlation between the magnetic and electric fields and some estimates for the dependence of these characteristics on collision energy and impact parameter are investigated. A comparison of some observables, which are calculated within the HSD model with and without the electromagnetic fields, is presented in Sect. IV. The results are summarized in Sect. V.

II. ELECTROMAGNETIC FIELD EVOLUTION WITHIN THE HSD MODEL

To describe a collision of heavy ions let us start from the relativistic Boltzmann equation for an on-shell phase-

space distribution function $f \equiv f(x, p)$

$$p^\mu \frac{\partial}{\partial x^\mu} f = C[f] \quad (1)$$

where $C[f]$ is the collision integral and x, p are the 4-coordinate and 4-momentum of a particle. A background electromagnetic field may be taken into account by including an electromagnetic tensor $F_{\mu\nu}$ into Eq.(1) as

$$p^\mu \left(\frac{\partial}{\partial x^\mu} - F_{\mu\nu} \frac{\partial}{\partial p^\nu} \right) f = C[f], \quad (2)$$

where

$$eF_{\mu\nu} = \partial_\mu A_\nu - \partial_\nu A_\mu \quad (3)$$

with the electromagnetic 4-vector potential $A_\mu = \{\Phi, \mathbf{A}\}$. Note that the left-hand side of Eq.(2) is gauge invariant.

Let us rewrite (2) in terms of components of A_μ and generalize it to the case of a set of particles moving in a nuclear potential U . Then the equation for a test particle characterized by the distribution function $f \equiv f(\mathbf{r}, \mathbf{p}, t)$ may be presented as follows:

$$\begin{aligned} & \left\{ \frac{\partial}{\partial t} + \left(\frac{\mathbf{p}}{p_0} + \nabla_{\mathbf{p}} U \right) \nabla_{\mathbf{r}} \right. \\ & - \left. \left(\nabla_{\mathbf{r}} U + e \nabla \Phi + e \frac{\partial \mathbf{A}}{\partial t} - e \mathbf{v} \times (\nabla \times \mathbf{A}) \right) \nabla_{\mathbf{p}} \right\} f \\ & = C_{coll}(f, f_1, \dots, f_N) \end{aligned} \quad (4)$$

The strength of the magnetic \mathbf{B} and electric \mathbf{E} fields is, respectively,

$$\mathbf{B} = \nabla \times \mathbf{A}, \quad \mathbf{E} = -\nabla \Phi - \frac{\partial \mathbf{A}}{\partial t}. \quad (5)$$

One should note that the electromagnetic field generated by moving nuclei may be considered as an external field: the value of the electromagnetic field at a given point is determined by the global charge distribution of colliding nuclei and thus, in good approximation, independent of the local strong interaction dynamics. However, the presence of the electromagnetic field can affect the interactions among particles, which simultaneously carry electric and (possibly) color charges.

Using relations (5), the system (4) is reduced to a more familiar form:

$$\begin{aligned} & \left\{ \frac{\partial}{\partial t} + \left(\frac{\mathbf{p}}{p_0} + \nabla_{\mathbf{p}} U \right) \nabla_{\mathbf{r}} + \right. \\ & \left. (-\nabla_{\mathbf{r}} U + e \mathbf{E} + e \mathbf{v} \times \mathbf{B}) \nabla_{\mathbf{p}} \right\} f = C_{coll}(f, f_1, \dots, f_N) \end{aligned} \quad (6)$$

for particles of a charge e .

The HSD transport model is based on Kadanoff-Baym equations for Green's function accounting for the first order gradient expansion of the Wigner transformed Kadanoff-Baym equation [37–39]. The hadronic mean field in Eq.(4) is $U \sim Re(\Sigma^{ret})/2p_0$ where Σ^{ret} denotes the retarded selfenergy. The change of the hadron mass in the HSD model results in an additional term ahead of $\nabla_{\mathbf{p}}$ in (4) [40] but it is ignored in our consideration which focuses on electromagnetic effects.

Transport equations for a strongly interacting particle with electric charge e (Eq.4) are supplemented by the electromagnetic field equations

$$\nabla \times \mathbf{E} = -\frac{1}{c} \frac{\partial \mathbf{B}}{\partial t}, \quad \nabla \cdot \mathbf{B} = 0. \quad (7)$$

The general solution of the wave equations (7) with the charge distribution $\rho(\mathbf{r}, t) = en$ and electric current $\mathbf{j}(\mathbf{r}, t) = e\mathbf{v}$ are

$$\Phi(\mathbf{r}, t) = \frac{1}{4\pi} \int \frac{\rho(\mathbf{r}', t') \delta(t - t' - |\mathbf{r} - \mathbf{r}'|/c)}{|\mathbf{r} - \mathbf{r}'|} d^3 r' dt' \quad (8)$$

for the electromagnetic scalar potential $\Phi(\mathbf{r}, t)$ and

$$\mathbf{A}(\mathbf{r}, t) = \frac{1}{4\pi} \int \frac{\mathbf{j}(\mathbf{r}', t') \delta(t - t' - |\mathbf{r} - \mathbf{r}'|/c)}{|\mathbf{r} - \mathbf{r}'|} d^3 r' dt' \quad (9)$$

for the vector potential. For a moving point-like charge one gets

$$\rho(\mathbf{r}, t) = e \delta(\mathbf{r} - \mathbf{r}(t)), \quad \mathbf{j}(\mathbf{r}, t) = e \mathbf{v}(t) \delta(\mathbf{r} - \mathbf{r}(t)) \quad (10)$$

and, after integration of Eq.(9) using

$$\int_{-\infty}^{\infty} g(x) \delta(f(x)) dx = \sum_i \frac{g(x_i)}{|f'(x_i)|}, \quad (11)$$

we obtain:

$$\Phi(\mathbf{r}, t) = \frac{e}{4\pi\epsilon_0} \sum_i \frac{1}{R(t'_i)\kappa(t'_i)} \quad (12)$$

with the definitions

$$\begin{aligned} \mathbf{R}(t'_i) &= \mathbf{r} - \mathbf{r}(t'_i), \\ \kappa(t'_i) &= 1 - \frac{\mathbf{R}(t'_i) \cdot \mathbf{v}(t'_i)}{cR(t'_i)} = \left| \left(\frac{df}{dt'} \right)_{t'=t'_i} \right|. \end{aligned} \quad (13)$$

In (13) the times t'_i are solutions of the retardation equation

$$f(t') = t' - t + R(t')/c = 0. \quad (14)$$

By analogy, for the vector potential we get:

$$\mathbf{A}(\mathbf{r}, t) = \frac{e\mu_0}{4\pi} \sum_i \frac{\mathbf{v}(t'_i)}{R(t'_i)\kappa(t'_i)} \quad (15)$$

Thus, Eqs.(8) and (9) lead to the retarded Liénard-Wiechert potentials (12) and (15) acting at the point $\mathbf{R} = \mathbf{r} - \mathbf{r}'$ at the moment t . The electromagnetic potentials $\Phi(\mathbf{r}, t)$ and $\mathbf{A}(\mathbf{r}, t)$ are generated by every moving charged particle and describe generally the elastic Coulomb scattering as well as inelastic bremsstrahlung processes. Below we set $\epsilon_0 = \mu_0 = 1$ in Eqs.(12) and (15), respectively. The retarded electric and magnetic fields can be derived now from Eqs.(12) and (15) using (5) as follows:

$$\begin{aligned}\mathbf{E}(\mathbf{r}, t) &= \frac{e}{4\pi} \left(\frac{\mathbf{n}}{\kappa R^2} + \frac{-\mathbf{b}/c - [(\mathbf{n} \cdot \mathbf{v})\mathbf{n} - \mathbf{v}]/R}{\kappa^2 c R} \right)_{ret} \\ &- \frac{e}{4\pi} \left(\frac{(-\mathbf{v}(t')/c + \mathbf{n}(t'))(v^2/c - \mathbf{n} \cdot \mathbf{v} - R/c(\mathbf{n} \cdot \mathbf{b}))}{\kappa^3 c R^2} \right)_{ret},\end{aligned}\quad (16)$$

$$\begin{aligned}\mathbf{B}(\mathbf{r}, t) &= \frac{e}{4\pi} \left(\frac{\mathbf{v} \times \mathbf{n}}{\kappa R^2} + \left(\frac{\mathbf{b}(t') \times \mathbf{n}(t') + \mathbf{v}(t') \times [(\mathbf{n} \cdot \mathbf{v})\mathbf{n} - \mathbf{v}]/R}{\kappa^2 c R} \right) \right)_{ret} \\ &- \frac{e}{4\pi} \left(\frac{(\mathbf{v}(t') \times \mathbf{n}(t'))(v^2/c - \mathbf{n} \cdot \mathbf{v} - R/c(\mathbf{n} \cdot \mathbf{b}))}{\kappa^3 c R^2} \right)_{ret}\end{aligned}\quad (17)$$

with the acceleration $\mathbf{b} = d/dt' \mathbf{v}$ and the unit vector $\mathbf{n} = \mathbf{R}/R$. After simplification and neglecting the acceleration \mathbf{b} we arrive at

$$e\mathbf{E} = \frac{\text{sign}(e)\alpha \mathbf{R}(t)(1-v^2/c^2)}{[(\mathbf{R}(t) \cdot \mathbf{v}/c)^2 + R^2(t)(1-v^2/c^2)]^{3/2}}, \quad (18)$$

$$e\mathbf{B} = \frac{\text{sign}(e)\alpha [\mathbf{v} \times \mathbf{R}(t)](1-v^2/c^2)}{c[(\mathbf{R}(t) \cdot \mathbf{v}/c)^2 + R^2(t)(1-v^2/c^2)]^{3/2}} \quad (19)$$

where in the left-hand side an additional charge e is introduced to get the electromagnetic fine-structure constant $\alpha = e^2/4\pi = 1/137$ in the right-hand side of these equations. The last expression is reduced to the familiar form of the retarded Liénard-Wiechert equation for the magnetic field of a moving charge

$$\mathbf{B}(\mathbf{r}, t) = \frac{e}{4\pi} \frac{[\mathbf{v} \times \mathbf{R}]}{cR^3} \frac{(1-v^2/c^2)}{[1-(v/c)^2 \sin^2 \phi_{Rv}]^{3/2}}, \quad (20)$$

with $\mathbf{R} = \mathbf{R}(t)$, ϕ_{Rv} is the angle between $\mathbf{R}(t)$ and \mathbf{v} .

The set of transport equations (4) in the following is solved in a quasiparticle approximation by using the Monte-Carlo parallel ensemble method. To find the electromagnetic field, a space grid is used. The quasiparticle propagation in the electromagnetic field is calculated according to Eq.(6) as

$$\frac{d\mathbf{p}}{dt} = e\mathbf{E} + \frac{e}{c}\mathbf{v} \times \mathbf{B}. \quad (21)$$

The change of the electromagnetic energy is $(e/c)(\mathbf{v} \cdot \mathbf{E})$ *i.e.* the magnetic field does not change the quasiparticle energy. To avoid singularities and self-interaction effects, particles within a given Lorentz-contracted cell are excluded from the field calculation.

III. RESULTS

The scheme described above for the computation of the electromagnetic field is applied here to ultra-relativistic heavy-ion collisions. However, for transparency, we shall start with the magnetic field created by a single freely

moving charge. As seen in Fig. 1, the charge creates a cylindrically symmetric field with the symmetry axis along the direction of motion. If one follows the magnetic field direction, it appears to be torqued around the direction of motion. Therefore, the magnetic field on the left and right sides with respect to the moving charge has opposite signs, resulting in some maximum and minimum of the magnetic field at a given instant of time. The opposite field signs directly follow from Eq.(20) if one takes into account that the vector \mathbf{R} (Eq.(13)) in this situation has opposite signs.

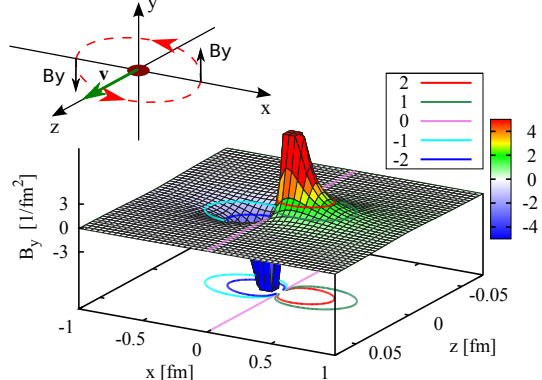


FIG. 1: (Color online) Snapshot of the B_y distribution for the magnetic field and its projection on the $(z-x)$ plane for a single charge moving along the z axis.

In a nuclear collision, the magnetic field will be a superposition of solenoidal fields from different moving charges. The collision geometry for a peripheral collision is shown in Fig. 2 in the transverse plane. The overlapping strongly interacting region (participants) has an “almond”-like shape. The nuclear region outside this almond (shaded in Fig. 2) corresponds to spectator matter which is the dominant source of the electromagnetic field at the very beginning of the nuclear collision. Note that in the HSD code the particles are subdivided into target and projectile spectators and participants not geometrically but dynamically: spectators are nucleons which suffered yet no collision.

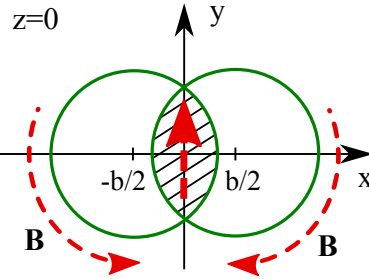


FIG. 2: (Color online) The transverse plane of a noncentral heavy-ion collision. The impact parameter of the collision is denoted by b . The magnetic field is plotted by the dashed lines.

A. Space-time evolution of the magnetic field

The time evolution of $eB_y(x, y = 0, z)$ for Au+Au collisions for the colliding energy $\sqrt{s_{NN}} = 200 GeV at the impact parameter $b = 10 fm is shown in Fig. 3. If the impact parameter direction is taken as the x axis (as in the present calculations), then the magnetic field will be directed along the y -axis perpendicularly to the reaction plane ($z - x$). The geometry of the colliding system at the moment considered is demonstrated by points in the ($z - x$) plain where every point corresponds to a spectator nucleon. It is seen that the largest values of $eB_y \sim 5m_\pi^2$ are reached in the beginning of a collision for a very$$

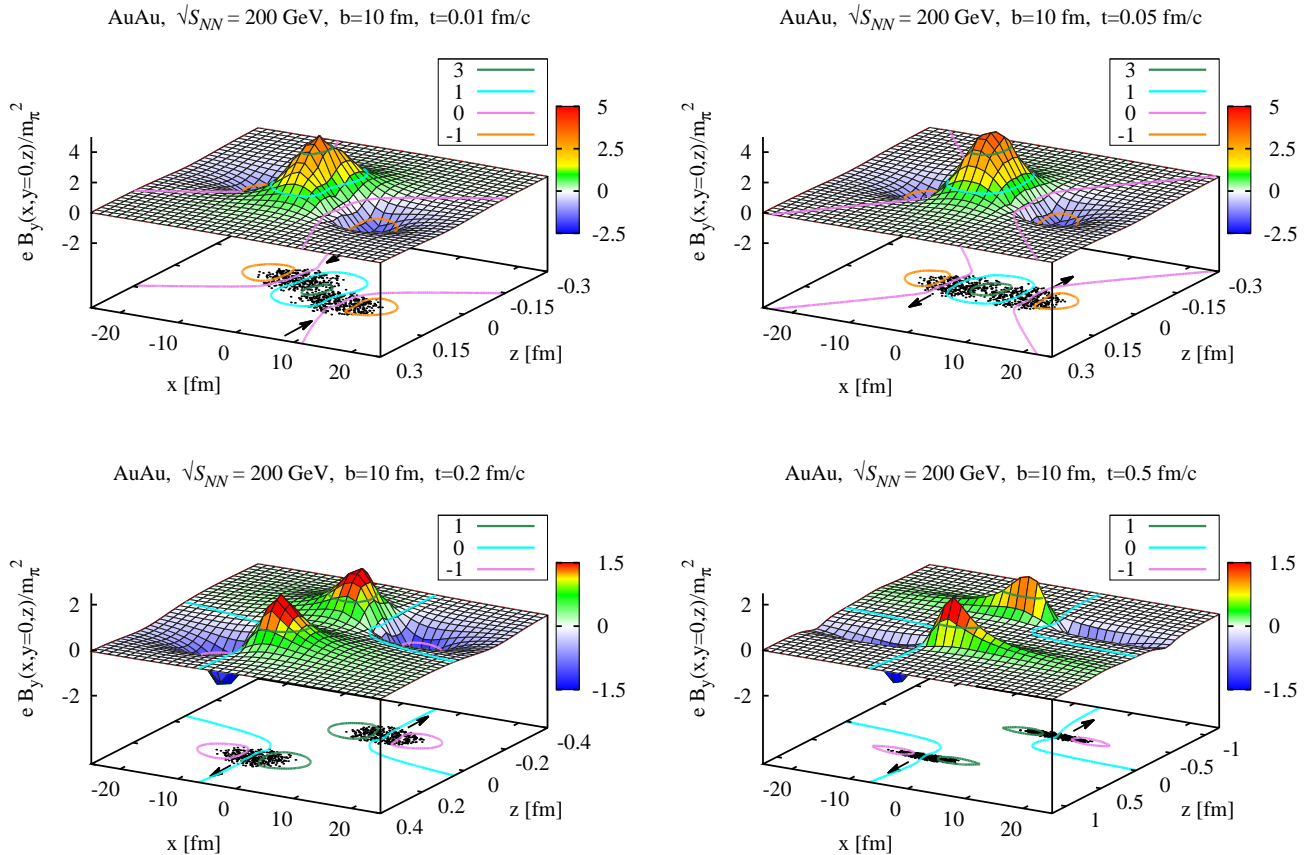


FIG. 3: (Color online) Time dependence of the spatial distribution of the magnetic field B_y at times t created in Au+Au ($\sqrt{s}=200$ GeV) collisions with the impact parameter $b=10$ fm. The location of spectator protons is shown by dots in the ($x - z$)-plane. The level $B_y = 0$ and the projection of its location on the ($x - z$) plane are shown by the solid lines.

short time corresponding to the maximal overlap of the colliding ions. Note that this is an extremely high magnetic field, since $m_\pi^2 \approx 10^{18}$ gauss. The first panel in Fig. 3 is taken at a very early compression stage with

$t = 0.01$ fm/c. The time $t = 0.05$ fm/c is close to the maximal overlapping and the magnetic field here is maximal. Then, the system expands (note the different z -scales in different panels of Fig. 3) and the magnetic field

decreases. For $b=0$ the overlapping time is maximal and roughly given by $2R/\gamma_c$ which for our case is about 0.15 fm/c. For peripheral collisions this time is even shorter.

Globally, the spatial distribution of the magnetic field is evidently inhomogeneous and Lorentz-contracted along the z -axis. At the compression stage there is a single maximum which in the expansion stage is splitted into two parts associated with the spectators. In the transverse direction the bulk magnetic field is limited by two minima coming from the torqued structure of the single-charge field (see Fig. 1).

The possibility of attaining extremely high magnetic fields in heavy-ion collisions was pointed out 30 years ago [41] but there have been only two real attempts to estimate the magnetic field for relativistic heavy-ion collisions [21, 26]. In Ref. [21] the colliding ions were treated as infinitely thin layers (pancake-like), and the results in the center of a Au-Au collision $eB_y(0,0,z)$ could be presented in a semi-analytical form. In Fig. 4 these estimates are confronted with our results. It is clearly seen

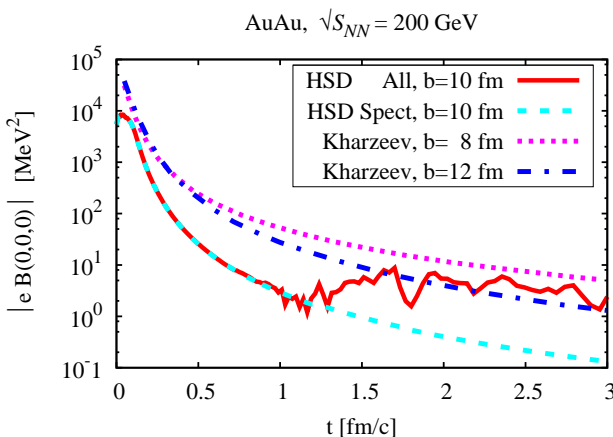


FIG. 4: (Color online) Time dependence of the $|eB|$ field in the center of the nuclear overlap region for Au+Au($\sqrt{s}=200$ GeV) collisions from the HSD calculations. The dotted and dot-dashed curves are from Ref. [21] at the impact parameters $b=8$ and 12 fm, respectively.

that the magnetic field in our transport model for $b=10$ fm is lower than the estimate from Ref. [21] for both $b=12$ and 8 fm. This difference originates mainly from the fact that to simulate rapidity degradation of pancake-like nuclei, a heuristic function was assumed with making no difference between surviving baryons and new created particles [21] whereas in our case the dynamical hadron-string model is used for both primary and subsequent interactions while keeping electric and baryonic charges and energy-momentum conservation [36]. The approximation of Ref. [21] is reasonable for first collisions but gets progressively worse with interaction time as seen in Fig. 4. The difference in the shape of the time dependence of the magnetic field for early times is due to neglecting the finite size of the colliding nuclei in Ref. [21].

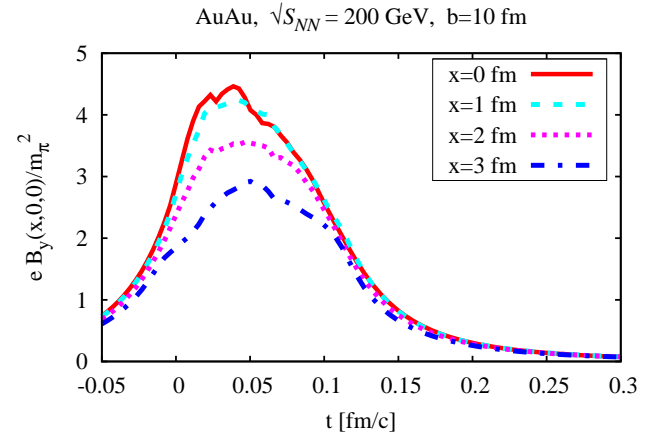


FIG. 5: (Color online) The magnetic field evolution at the point x for $y=0$.

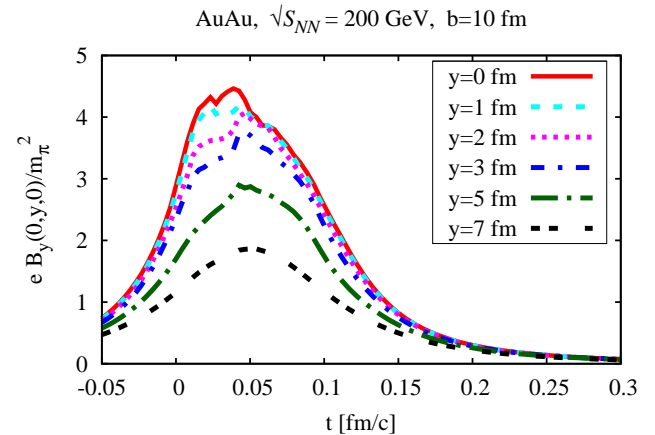


FIG. 6: (Color online) Time evolution of the magnetic field at the point y for the central overlap point $x=0$.

Also, in our treatment the self-interaction is excluded for charges within the Lorentz-contracted hadron volume. Our consideration treats more accurately the retardation effect discussed above which constrains the contributions to the given point from some charges. It is especially important for the field contribution from participants.

It is of interest to note that in our transport model, the spectator contribution to the magnetic field is practically vanishing at $t \approx 1$ fm/c (see Fig. 4). In subsequent times the magnetic field eB_y is formed essentially due to produced participants with roughly equal number of negative and positive charges which approximately compensate each other. The visible effect in our approach is by an order of magnitude lower than that in the estimate [21] which demonstrates the essential role of the retardation in this interaction phase.

Furthermore, the magnetic field distribution in [26] is calculated within the UrQMD model and the back reaction of the field on particle propagation is disregarded. Nevertheless, our results are quite close to those

of Ref. [26].

In Fig. 5, the magnetic field evolution $eB_y(x, y = 0, z)$ is shown as a function of the transverse coordinate x . Practically the difference between results for $x = 0, 1, 2$ fm is less than 20% except for the boundary of the overlap region corresponding to $x \approx b/2 \sim 5$ fm. One thus may conclude that the magnetic field is rather homogeneous in the transverse direction.

The magnetic field component $B_y(x = 0, y, z)$ along the largest axis y of the “almond” (see Fig. 2) is presented in Fig. 6 for different times. The similarity of all curves

for $y \lesssim 4$ demonstrates a high homogeneity of the created field B_y . It is of interest that this field stays almost constant during $\Delta t \sim 0.1$ fm/c.

B. Energy density and its correlation with B_y

Along with a high magnetic field, the presence of a quark-gluon phase is a necessary condition for a manifestation of the chiral magnetic effect according to

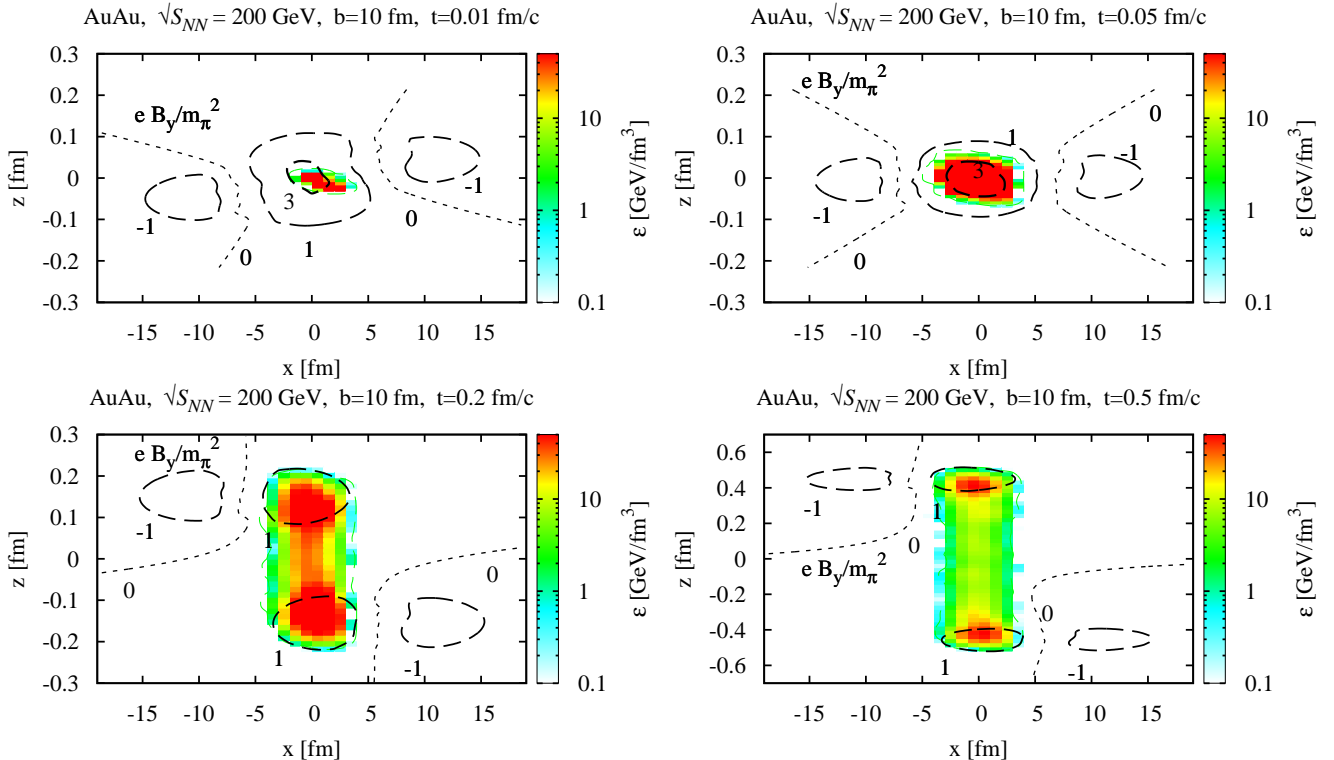


FIG. 7: (Color online) Spatial correlations in location of the magnetic field and energy density of participants produced in Au+Au($\sqrt{s} = 200$ GeV) collisions with the impact parameter $b = 10$ fm at the times t . The levels of the magnetic field are plotted by dashed lines whereas areas with different energy densities are displayed in color.

Refs. [15, 19–23]. The phase structure of excited matter is essentially defined by the energy density (cf. Ref. [42]). One can expect that for energy densities $\epsilon \gtrsim 1$ GeV/fm 3 the system is in a deconfined phase. The evolution of the energy density of created particles is presented in Fig. 7. Here the maximal energy density (in the center of the colliding system) is $\epsilon > 50$ GeV/fm 3 at the moment of maximal overlap of the nuclei. When the system expands, it takes a sausage-like shape (or dumb-bell shaped if the energy density values are taken into consideration additionally) and the energy density drops fast. But even at the time $t \sim 0.5$ fm/c (last panel in Fig. 7) the local

energy density is seen to be above an effective threshold of a quark-gluon phase transition $\epsilon \gtrsim 1$ GeV/fm 3 . Different levels of the magnetic field strength are plotted in the same figure. It is clearly seen that the location of the maximum energy density correlates with that for the magnetic field.

The variation of the energy density distribution with the transverse coordinate x is shown in Fig. 8. Here the plotted values of ϵ correspond to averages within the Lorentz-contracted cylinder with $|z| < 5/\gamma$ fm and radius $R = 1$ fm centered at the point x . One can see that the energy density changes more strongly in x than the

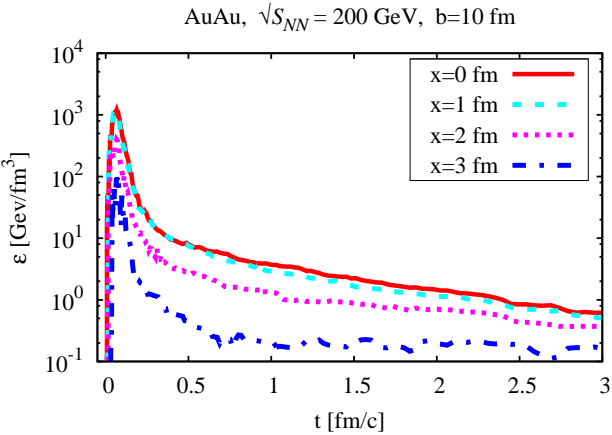


FIG. 8: (Color online) The average energy density in the Lorentz-contracted cylinder of the radius $R = 1$ fm and $|z| < 5/\gamma$ fm with the z -axis passing through the point x .

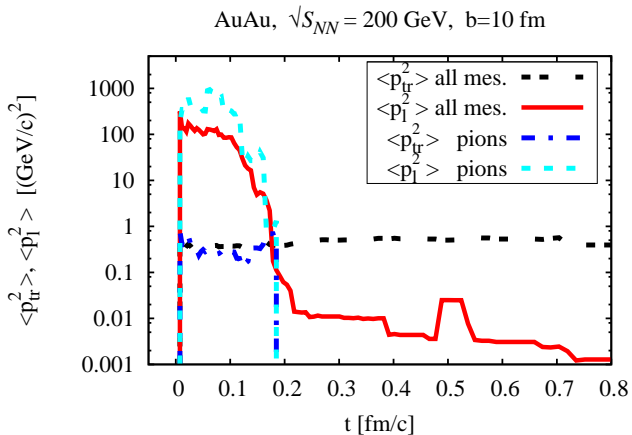


FIG. 9: (Color online) The average longitudinal and transverse momenta of all mesons and pions in the Lorentz-contracted cylinder described above.

magnetic field (note the logarithmic scale in Fig. 8). In particular, the maximal ε decreases by a factor ~ 20 when one proceeds from $x = 0$ to $x = 3$ fm and close to the spectator-participant boundary (at $x \approx 3$ fm) the energy density very quickly (within roughly ~ 0.3 fm/c) drops below the effective threshold for deconfinement $\varepsilon \sim 1$ GeV/fm³.

One should note that the energy density should be calculated in the rest system. The choice of a symmetric position of the cylinder volume with respect to the $z=0$ plane essentially leads to an approximately vanishing total momentum of particles inside this volume. The time averaged γ -factor of particles in this cylinder in the c.m. system is $\langle \gamma \rangle \sim 1.1$. Note, however, that the created particles are not in local equilibrium!

In Fig. 9 the evolution of the average longitudinal $\langle p_l \rangle$ and transverse $\langle p_{tr} \rangle$ momentum is shown for mesons in the same cylinder. All mesons keep a constant

transverse momentum $\langle p_{tr} \rangle$ during the whole evolution even if the fastest pions escape the finite cylinder volume by the time $t \sim 0.2$ fm/c. The ratio $\langle p_l \rangle / \langle p_{tr} \rangle$ is very large and does not correspond to that in equilibrium. The sharp decrease of $\langle p_l \rangle$ in time is due to fast mesons streaming-out from the finite volume due to the longitudinal expansion of the system rather than to equilibration. Thus, in the early stage $t \lesssim 0.2$ fm/c the Au+Au system with high energy density is far from equilibrium. On the one hand, this fact is not astonishing since this stage should be treated in terms of quarks and gluons rather than on a hadronic level (cf. corresponding PHSD studies [42]). On the other hand, there is a general consensus that local equilibrium hydrodynamics can be applied to heavy-ion reactions at energies currently available the BNL Relativistic Heavy Ion Collider (RHIC) only for $t > t_0 \approx 0.5$ fm/c [43, 44].

C. Electric field evolution

The background electric field, being orthogonal to the magnetic one, is directed along the x axis. The evolution of the eE_x field for peripheral ($b = 10$ fm) collisions of Au+Au at the top RHIC energy is presented in Fig. 10. Similar to the case of the magnetic field, the $eE_x(x, y = 0, z)$ distribution is also inhomogeneous and closely correlates with geometry while the field strength looks “hedgehog” shaped. When the two nuclei collide, the electric fields in the overlap region significantly compensate each other, and the electric field \mathbf{E} in the target and projectile spectator parts have opposite signs. As a result, the locations of the maximum/minimum are not in the central point of the overlap region - as they are for the magnetic field - but shifted slightly outside. The maximum of the electric field can be quite large. All these features are seen explicitly in Fig. 11 where the temporal evolutions of $eE_x(x, 0, 0)$ and $eE_y(x, 0, 0)$ are given for different values of the transverse coordinate x . Due to destructive interference or the “hedgehog” effect, the electric field in the central part of the overlap region ($x \approx 0$ fm) is consistent with zero apart from a short period just before reaching maximal overlap. For $x \simeq 1-3$ fm the electric field has a distinct maximum of $eE_x/m_\pi^2 \approx (0.5-0.6)$ which is only by a factor of about 10 less than the maximal magnetic field eB_y (cf. Fig. 5). But when moving farther away from the center of the overlap region the eE_x component drops sharply and then becomes negative. The eE_y field component is quite small for the central part of the overlap region and increases slightly for larger x . Note that the electric field is negligible for $t \gtrsim 0.15$ fm/c.

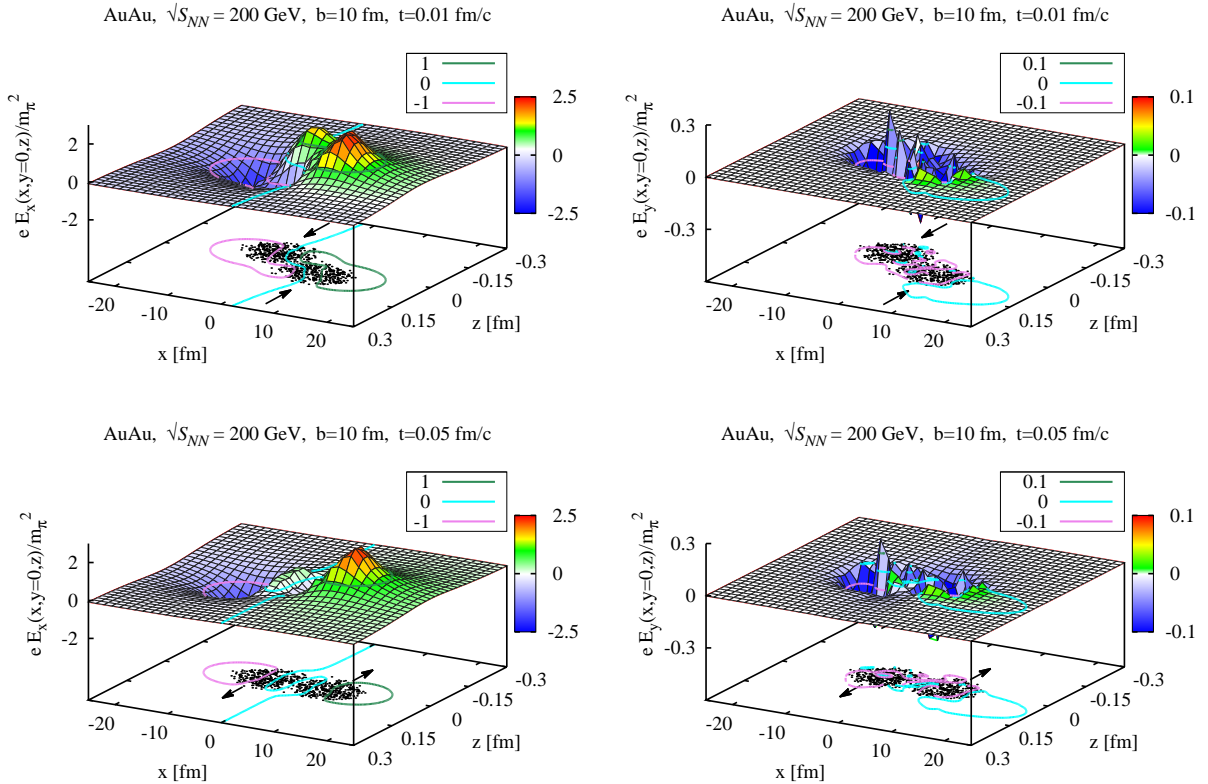


FIG. 10: (Color online) Evolution of the x - and y -components of the electric field at incoming and maximal overlap in Au+Au($\sqrt{s}=200$ GeV) collisions at the impact parameter $b=10$ fm. The $eE_x=\text{const}$ levels and spectator points are shown in the projection on the $(x-z)$ plane.

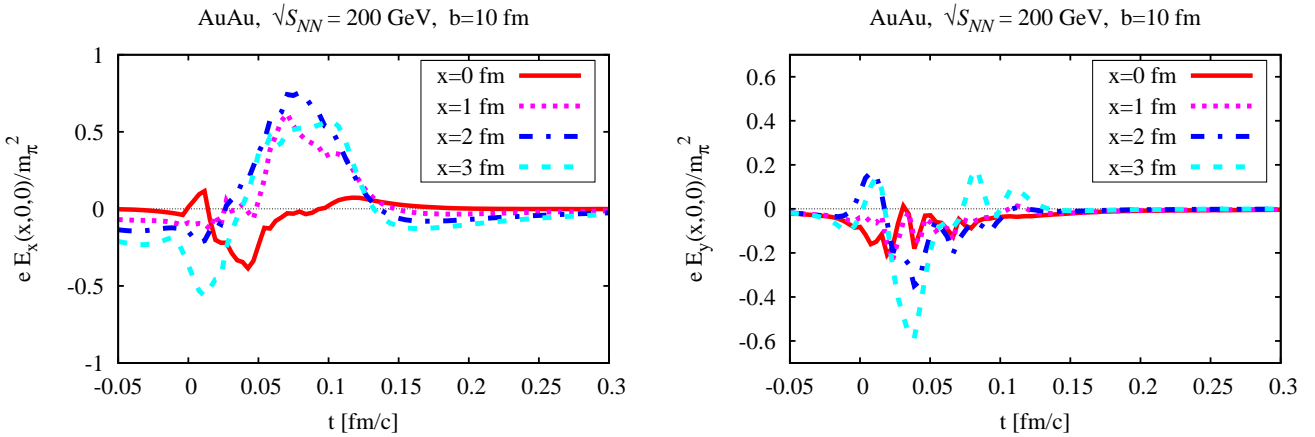


FIG. 11: (Color online) Evolution of the x (left panel)- and y (right panel)-components of the electric field for different values of the transverse coordinate x .

D. Scalar product of $(\mathbf{E} \cdot \mathbf{B})$

Since the magnetic field is odd under time reversal (or equivalently, under the combined charge conjugation and parity \mathcal{CP} transformation), the time reversal symmetry of a quantum system is broken in the presence of an ex-

ternal magnetic field. A magnetic field \mathbf{B} can also combine with an electric field \mathbf{E} to form the Lorentz invariant $(\mathbf{E} \cdot \mathbf{B})$ which changes the sign under a parity transformation. In the normal QCD vacuum with its spontaneously broken chiral symmetry the leading interaction involves the invariant $(\mathbf{E} \cdot \mathbf{B})$ which enters *e.g.* into the

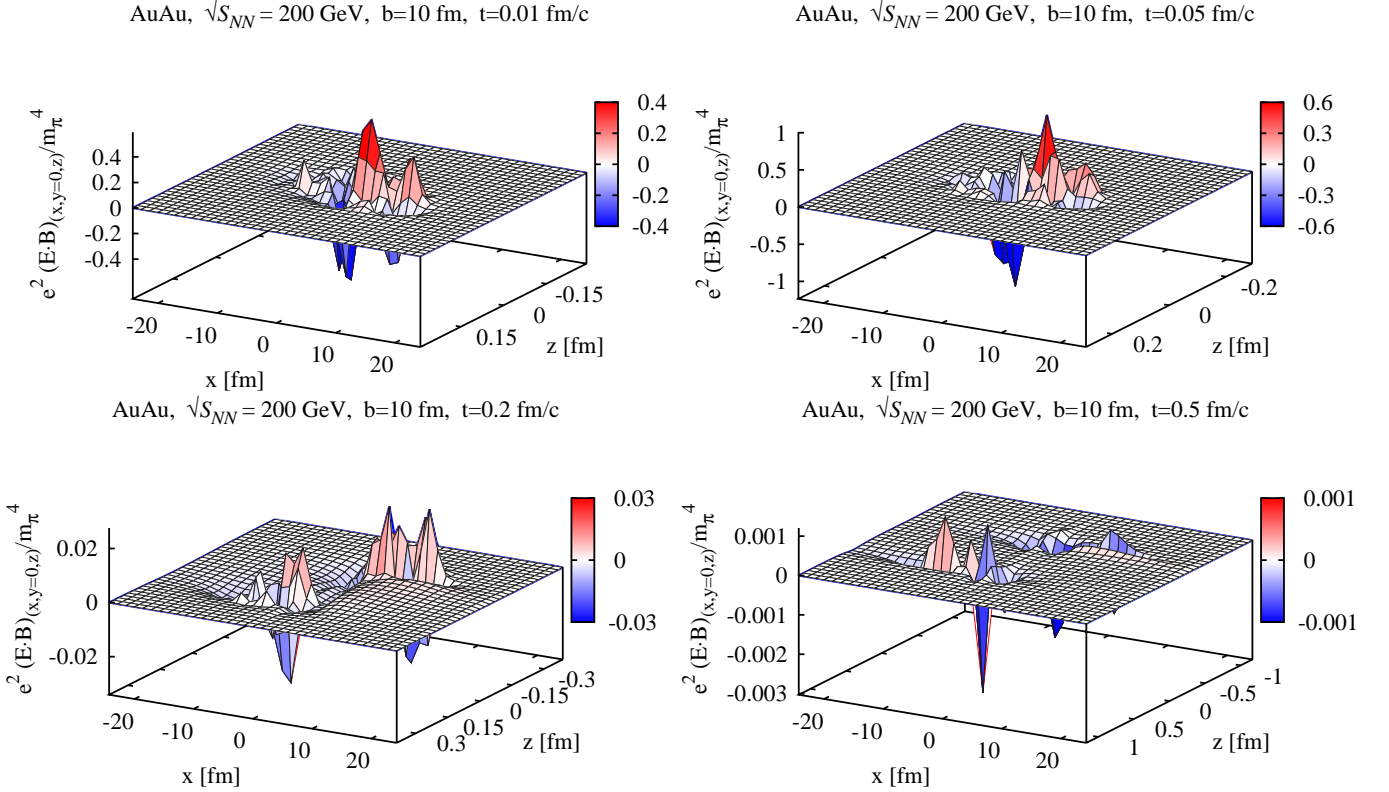


FIG. 12: (Color online) Space-time evolution of the scalar product of electric and magnetic field ($\mathbf{E} \cdot \mathbf{B}$) for a Au+Au reaction with the impact parameter $b = 10$ fm at $\sqrt{s} = 200$ GeV.

matrix element that mediates the two-photon decay of the neutral pseudoscalar mesons. In the deconfined chirally symmetric phase of QCD, the leading interaction term is proportional to $\alpha\alpha_s(\mathbf{E} \cdot \mathbf{B})(\mathbf{E}^a \cdot \mathbf{B}^a)$, where \mathbf{E}^a and \mathbf{B}^a denote the chromoelectric and chromomagnetic fields, respectively, and α and α_s are the electromagnetic and strong QCD couplings. Both interactions are closely related to the electromagnetic axial anomaly, which in turn relates the divergence of the isovector axial current to the pseudoscalar invariant of the electromagnetic field (see Ref. [45]). The evolution of the electromagnetic invariant - produced in Au+Au ($\sqrt{s}=200$ GeV) collisions at the impact parameter $b = 10$ fm - is shown in Fig. 12.

As seen the electromagnetic invariant ($\mathbf{E} \cdot \mathbf{B}$) is non-zero only in the initial time $t \lesssim 0.5$ fm/c where the ($\mathbf{E} \cdot \mathbf{B}$) distribution is quite irregular and its non-zero values correlate well with the location of the overlap region. For longer times this electromagnetic invariant vanishes as follows from the electric field space-time distributions (cf. Figs. 10 and 11). Note that the quantities plotted in Fig. 12 are dimensionless and the scaling factor m_π^4 [GeV⁴] is quite small. In a topological domain the chromoelectric fields ($\mathbf{E}^a \cdot \mathbf{B}^a$) $\neq 0$. But here non-vanishing values of the electromagnetic invariant are due to highly inhomogeneous distributions of electromagnetic fields \mathbf{E} and \mathbf{B} .

E. Impact parameter dependence

As noted above, the electromagnetic field is formed predominantly by spectators during the passage time of the two colliding nuclei. Since the number of spectators increases with the impact parameter b , the magnetic field should also increase for more peripheral collisions. Indeed, as seen in Fig. 13, the magnetic field decreases

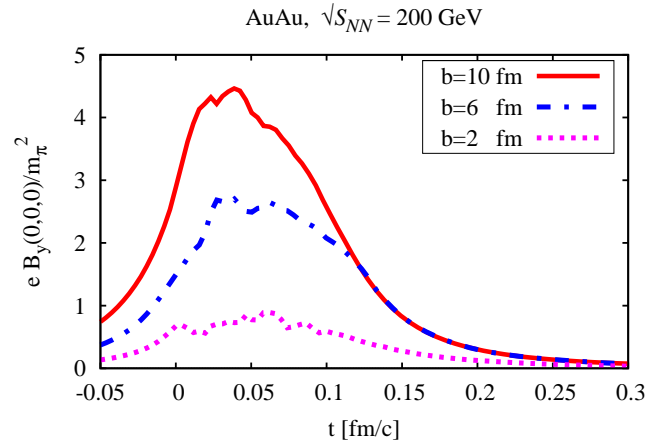


FIG. 13: (Color online) Impact parameter dependence of the magnetic field in Au+Au collisions at $\sqrt{s_{NN}} = 200$ GeV.

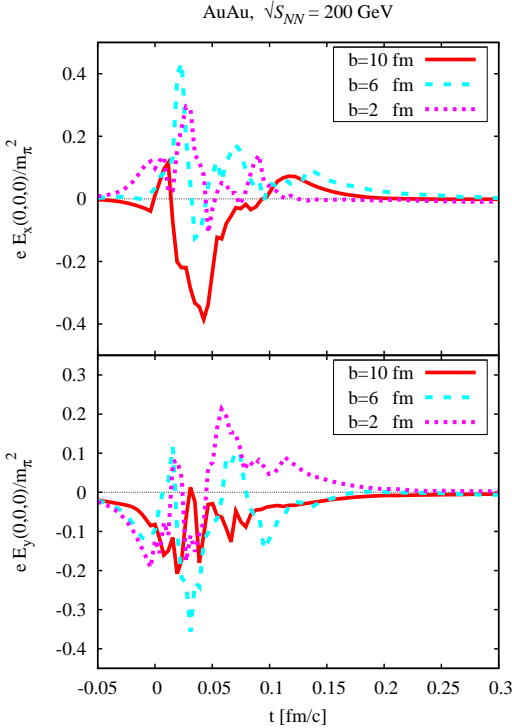


FIG. 14: (Color online) Impact parameter dependence of the $eE_x(x = 0, 0, z)$ (top panel)- and $eE_y(x = 0, 0, z)$ (bottom panel)- components of the electric field in Au+Au collisions at $\sqrt{s_{NN}} = 200$ GeV.

gradually with decreasing b . When changing the impact parameter from $b = 10$ to 2 fm, the maximal $eB_y(x, 0, 0)$ decreases by a factor of 5. For $t \gtrsim 0.3$ fm/c the magnetic field goes down almost exponentially (cf. with Fig. 4).

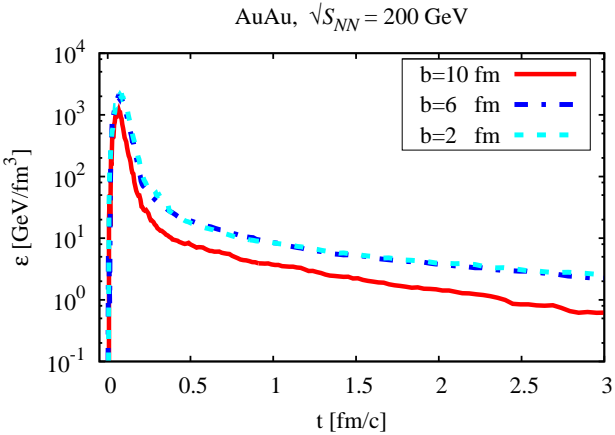


FIG. 15: (Color online) Impact parameter dependence of the average energy density in the Lorentz-contracted cylinder of radius $R = 1$ fm and $|z| < 5/\gamma$ fm with the z -axis passing through the point $x = 0$ in Au+Au collisions at $\sqrt{s_{NN}} = 200$ GeV.

For the electric field, the eE_x -component is only slightly

above the eE_y -component; both are constrained to the time interval $0 \lesssim t \lesssim 0.2$ fm/c (Fig. 14). Irregularities in these distributions are due to the “hedgehog” effect mentioned above.

In contrast, the impact dependence of the energy density ϵ should correlate with the number of participants and therefore reach a maximum in central collisions. The b -dependence of the ϵ temporal distributions is quite weak (see Fig. 15), and it decreases (by a factor of ~ 2) only for far peripheral collisions, $b \sim 10$ fm.

Note that in the $(x - z)$ plane, the location of the maximal values of the magnetic field and the energy density correlate with each other (see Fig. 7).

F. Dependence on collision energy

In principle, the collision energy dependence of electric and magnetic fields is given by Eqs. (16) and (17), respectively, since the fields predominantly emerge from spectators moving with the initial velocity v . These expressions involve velocity-dependent factors v and $1 - v^2$, which vanish in the limiting cases $v \rightarrow 0$ or $v \rightarrow 1$. In any of these limiting cases, the denominators stay finite and the energy dependence is given by the numerator. So, the electric field approaches zero in the ultrarelativistic limit $v \rightarrow 1$; the magnetic field vanishes in both limits $v \rightarrow 0$ and $v \rightarrow 1$. As follows from Fig. 16, the maximal strength

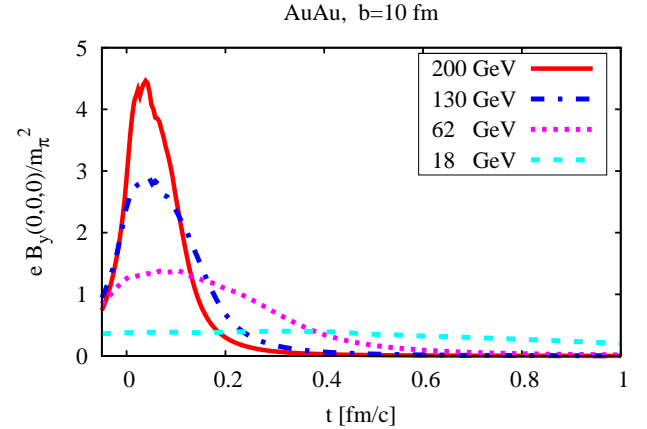


FIG. 16: (Color online) Collision energy dependence of the magnetic field evolution in the center point of the overlap region.

of the magnetic field $eB_y(0, 0, 0)$ decreases roughly proportionally to $\sqrt{s_{NN}}$ and at the top energy available at the CERN Super Proton Synchrotron (SPS) ($\sqrt{s_{NN}} \approx 18$ GeV), it is only about $\sim 0.4/m_\pi^2$ which appears to be too low to search for the Chiral Magnetic Effect [27]. One should keep in mind that the chiral magnetic effect depends not only on the magnitude of the magnetic field but also on the time of the system within the high magnetic field. As seen in Fig. 16, with decreasing collision energy

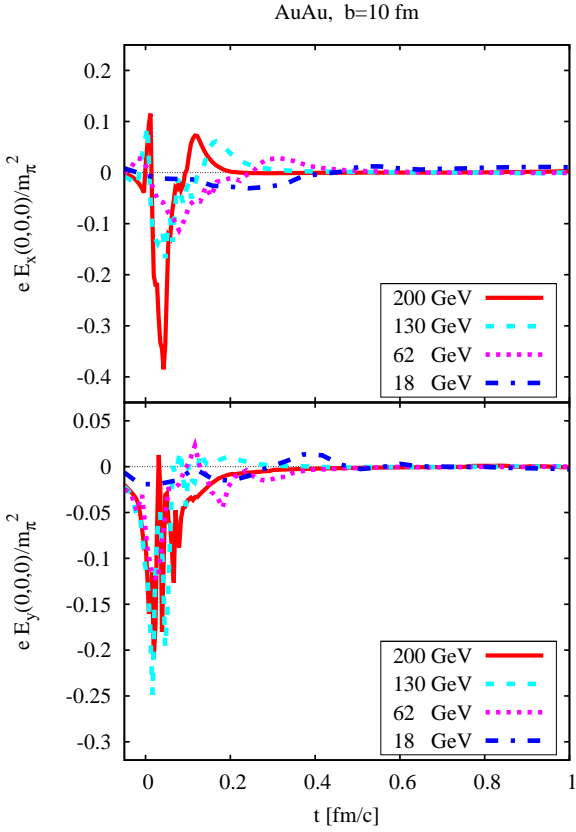


FIG. 17: (Color online) Collision energy dependence of the x and y component of the electric field.

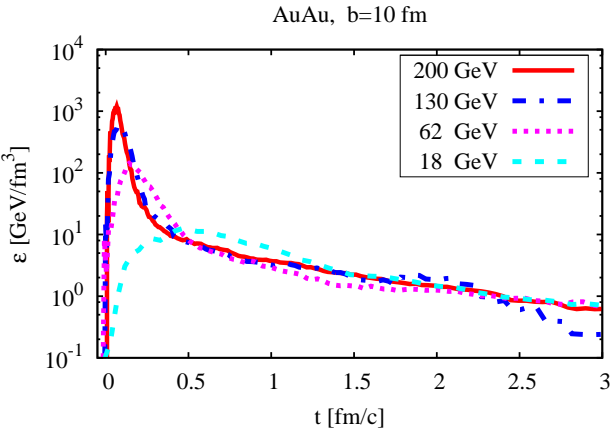


FIG. 18: (Color online) Collision energy dependence of the average energy density in the Lorentz-contracted cylinder of radius $R = 1$ fm and $|z| < 5/\gamma$ fm with the z -axis passing through the point $x = 0$.

the width of the time distribution of B_y becomes wider because it is defined essentially by the Lorentz-contracted overlap region $\sim \Delta r/\gamma = 2m_N\Delta r/\sqrt{s_{NN}}$. The RHIC energy is not high enough to see the limiting case corresponding to $(1 - v^2) \rightarrow 0$.

According to our expectation, the maximal strength of the $eE_x(0, 0, 0)$ and $eE_y(0, 0, 0)$ components decrease for lower collision energy as demonstrated in Fig. 17. It is clearly seen by comparing the results for $\sqrt{s_{NN}} = 200$ and 18 GeV. Note that the eE_y component is directed opposite to the direction of the magnetic field eB_y and will act against “the electric charge separation effect” [20, 21, 46].

The maximal energy density drops down by two orders of magnitude when going down from the RHIC to the SPS energy (see Fig. 18). During the time interval $0.5 \lesssim t \lesssim 2.5$ the energy density $\varepsilon(t)$ evolution for all energies practically coincide changing from $\varepsilon \sim 10$ to ~ 1 GeV/fm 3 .

IV. OBSERVABLES AND ELECTRIC CHARGE SEPARATION

The HSD model quite successfully describes many observables in a large range of the collision energy [36, 47]. Here we investigate to what extent the electromagnetic field - incorporated in the HSD approach - will affect some observables. We shall limit ourselves to Au+Au collisions at $\sqrt{s_{NN}} = 200$ GeV and impact parameter $b = 10$ fm. In this case we are not able to restrict our calculations to times $t < 3$ fm/c as above but have to calculate the whole nuclear interaction including the decays of resonances at least up to times of 50 fm/c.

The HSD results for the versions without and with electromagnetic field - taking into account the back reaction of the electrodynamic field on the particle propagation - are presented in Fig. 19. With a high degree of accuracy, we see no difference between these two versions in the transverse mass m_t and rapidity y .

In Fig. 20 the transverse momentum dependence of the elliptic flow of charged pions is compared for two versions (with and without field) of the HSD model. We do not observe any significant difference between the two cases. Slight differences are seen in the range of $p_t \sim 1$ GeV/c but certainly it can not be considered as significant. Note that generally the HSD model underestimates the elliptic flow, but an inclusion of partonic degrees of freedom within the PHSD approach allows it to describe perfectly well the p_t dependence of v_2 at the top RHIC energy [42].

As a signal of possible \mathcal{CP} violations in relativistic heavy-ion collisions, it was proposed in Ref. [46] to measure the two-particle angular correlation

$$\langle \cos(\phi_\alpha + \phi_\beta - 2\Psi_{RP}) \rangle \quad (22)$$

where Ψ_{RP} is the azimuthal angle of the reaction plane defined by the beam axis and the line joining the centers of colliding nuclei (see Fig.2). The correlator (22) is calculated on the event-by-event basis with subsequent averaging over the whole event ensemble. The experimental data from the STAR Collaboration [28, 29] and the results of HSD calculations are presented in Fig. 21. The experimental acceptance $|\eta| < 1$ and $0.15 < p_t < 2$

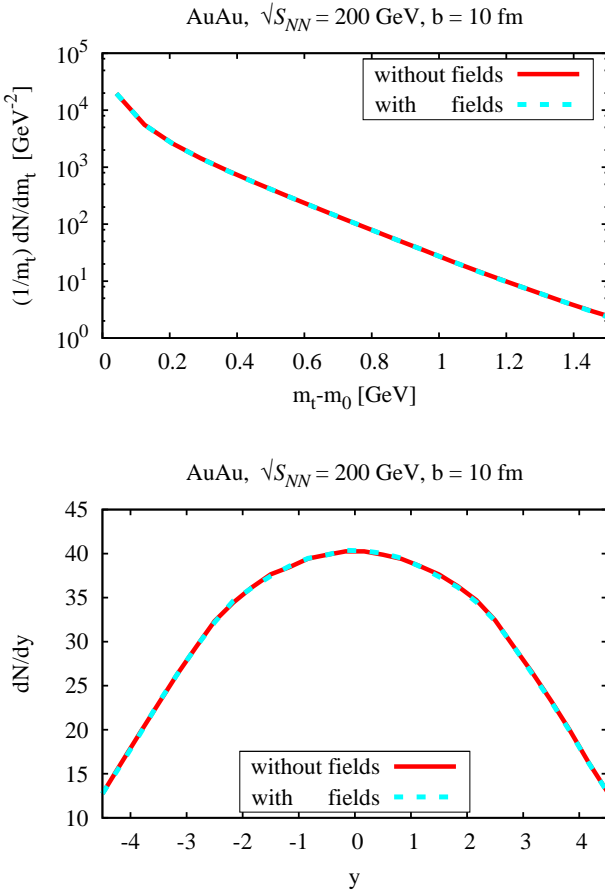


FIG. 19: (Color online) Transverse mass and rapidity distributions of charged pions produced in Au+Au ($\sqrt{s_{NN}} = 200$ GeV) collisions at $b = 10$ fm. The results calculated with and without electromagnetic field are plotted by the dotted and solid lines, respectively.

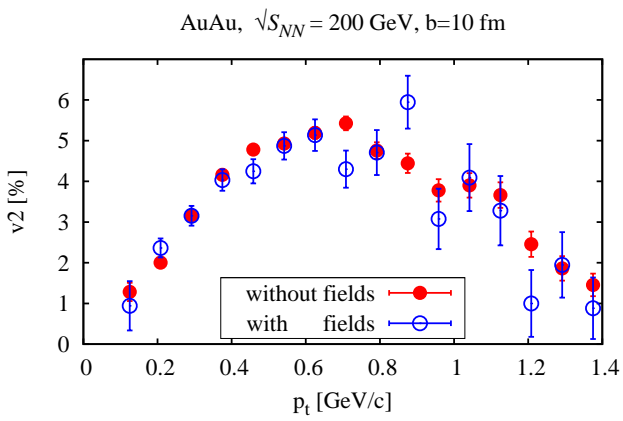


FIG. 20: (Color online) The transverse momentum dependence of the elliptic flow for Au+Au ($\sqrt{s_{NN}} = 200$ GeV) collisions at $b = 10$ fm.

GeV have been also incorporated in theoretical calcula-

tions. Note that the theoretical reaction plane is fixed exactly by the initial conditions and therefore is not defined by a correlation with a third charged particle as in the experiment [28, 29]. The error bars plotted in Fig.21 show the statistical errors. The number of events evalua-

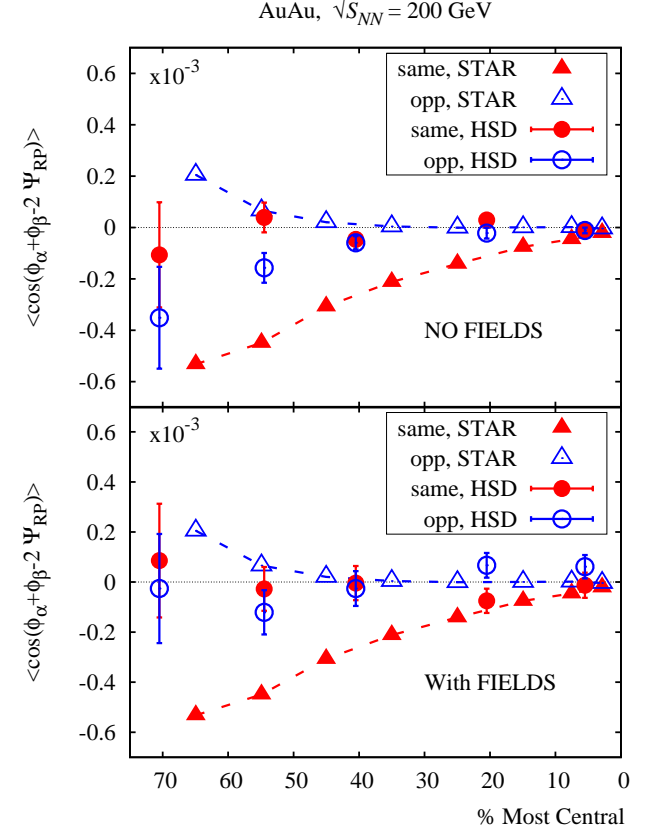


FIG. 21: (Color online) Azimuthal correlation in the transverse plane as a function of centrality for like and unlike charged pions from Au+Au ($\sqrt{s_{NN}} = 200$ GeV) collisions. The experimental points - connected by lines - are taken from [28, 29].

ated with (without) field for the most crucial centralities 0.7 and 0.55 are $6.8 \cdot 10^4$ and $2.2 \cdot 10^4$ ($8.4 \cdot 10^4$ and $5.4 \cdot 10^4$) for same charge pion pairs. The computational time for one event with accounting for the electromagnetic field is by a factor of about 30 longer than that for the case without field.

The expected CME stems from the interplay of topological effects of the excited vacuum and the chiral anomaly in the presence of a strong magnetic field [15, 20–23]. One can see that the calculated background - taking into account hadron string interaction dynamics and evolution of the electromagnetic field - is not able to describe the measured distribution especially for pions of the same charge. One should mention that our results are rather close to the background estimates within the UrQMD model in the experimental works [28, 29].

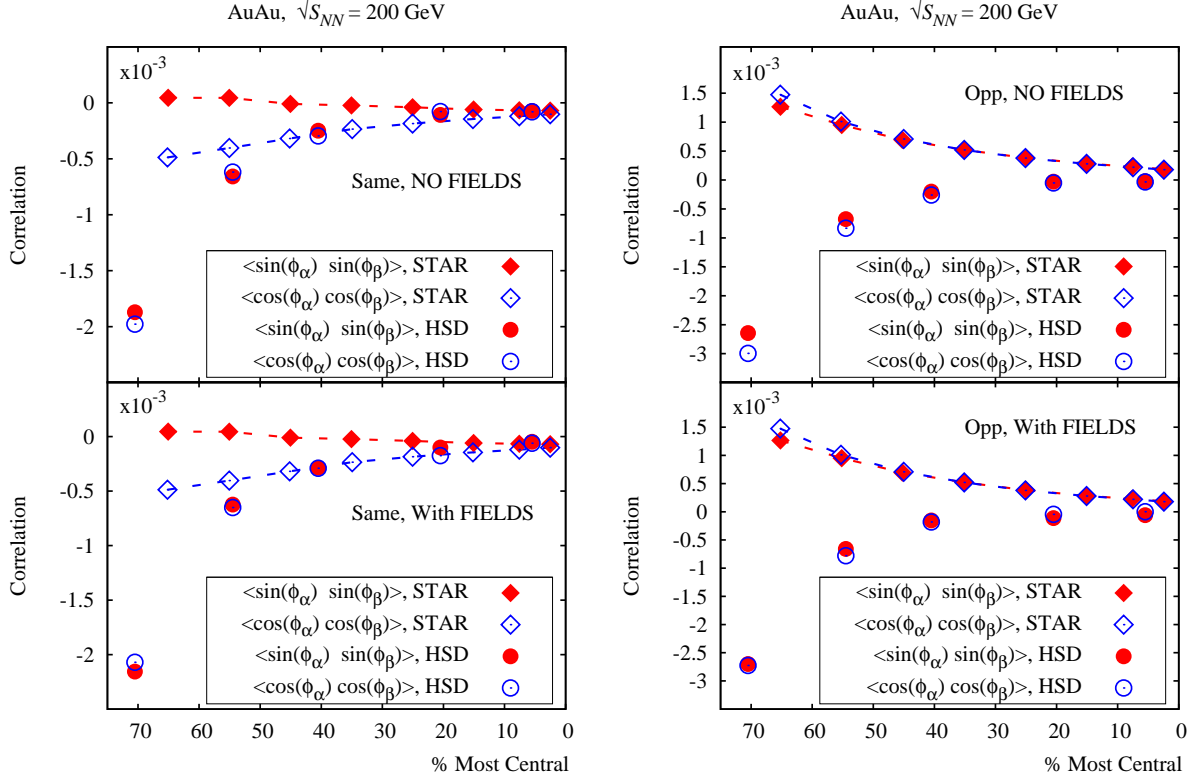


FIG. 22: (Color online) Projections of azimuthal correlations on the in- and out-reaction plane as a function of centrality for like and unlike charge pions from Au+Au ($\sqrt{s_{NN}} = 200$ GeV) collisions. The experimental points - connected by lines - are from Ref. [29].

The two particle correlation (22) can be decomposed in “in-plane” and “out-of-plane” components [52]

$$\langle \cos(\phi_\alpha + \phi_\beta) \rangle = \langle \cos(\phi_\alpha) \cos(\phi_\beta) \rangle - \langle \sin(\phi_\alpha) \sin(\phi_\beta) \rangle. \quad (23)$$

Following Ref. [32] in Fig. 22 these components are presented for the same $(+, +)$, $(-, -)$ and opposite $(+, -)$ charged pion pairs. First, there is no difference for HSD results without field (top panels in Fig. 22) and with the electromagnetic field included (bottom panels). To be more specific, we will discuss below the results with the electromagnetic field included. Second, the calculated difference between the in-plane (*cosine*-term) and out-of-plane (*sine*-term) components is small in the same and opposite charge cases.

Since the observed correlation (23) is the difference of these two terms, the calculated correlation is small as well. Furthermore, for the same charge pairs the measured *sine* term is essentially zero while the *cosine* term is finite. This implies that the observed correlations are in-plane rather than out-of-plane, as expected. It is of interest that the measured and calculated *cosine* terms coincide with each other for centralities $\lesssim 0.55$. As was noted in Ref. [32], the zero *sine* component is contrary

to the expectation from the CME, which for the same charge correlation results in an out-of-plane correlation. In the HSD model the *sine* term is not zero but negative. This is not a surprise because the induced chromoelectric field parallel to the out-of-plane B_y is not included into our calculations, but there is a nonzero electric field component E_y (see above). Furthermore, we see that for opposite charge pairs the *sine* and *cosine* correlation terms are virtually identical, which, according to Refs. [32, 33], is hard to reconcile with a sizable elliptic flow in these collisions. However, the centrality distributions of opposite charge pions exhibit contrary trends: the STAR measurement is positive and decreases but the HSD result is negative and increases toward central collisions where all components of angular correlations ≈ 0 . It is noteworthy that the UrQMD model shows quite close results. Indeed, $\langle \cos(\phi_\alpha - \phi_\beta) \rangle$ is just the sum of *cosine* and *sine* terms. So, summing the two opposite charge curves in Fig. 22 we reproduce the UrQMD results presented in Fig. 5 of Ref. [29].

Recently there were proposals to explain the observed CME effect without reference to the local parity violation. Different background mechanisms of the azimuthal correlation are considered: cluster decays, local transverse momentum conservation and local electric charge

conservation [30–33]. These mechanisms may contribute to the effect under discussion, but their simplified estimates made in these papers are not able to describe the STAR measurements. Generally speaking, all these effects, such as the decay of resonances including heavy ones and the exact conservation of electric charge and energy-momentum, are involved in our transport model but they do not help. However, there is a conflicting point here. The HSD model treats the system evolution for Au+Au(200 GeV) in terms of hadrons and strings while the decisive phenomena occur for times $t \lesssim 0.3$ fm/c. This is definitely in a non-equilibrium quark-gluon state. On the other hand, as was shown in the multi-phase model [48], the charge separation can be significantly reduced by the evolution of the quark-gluon plasma produced in relativistic heavy-ion collisions and by the subsequent hadronization process.

The conservation of the transverse momentum is a possible source of azimuthal correlations which was suggested to be a significant contribution to the measured observable (Eq. 22) [31–33]). Using Eq.(23) and the conservation of the transverse momenta, it was shown that roughly [31, 32])

$$\langle \cos(\phi_\alpha + \phi_\beta - 2\Psi_{RP}) \rangle \simeq -\frac{v_2}{N}, \quad (24)$$

where v_2 is the elliptic flow coefficient measured for all produced particles and N is the total number of all produced particles. It is definitely a qualitative result, but it demonstrates a close relation of the observed charge separation effect with the elliptic flow. Equation (24) was specified more accurately in Ref. [32]) and the correlator (22) was estimated under reasonable assumptions. It was concluded that transverse momentum conservation alone is not sufficient for explaining the STAR data. One should add that this issue has been considered in the multi-phase model [48] as well, with the conclusion that the charge particle separation leads to a modification of the relation between the charge azimuthal correlation and the elliptic flow that is expected from transverse momentum conservation (Eq. 24). An essential point from this discussion is that the charge separation effect is roughly proportional to the elliptic flow; however, this quantity is underestimated in the HSD model resulting in a small value of the correlator. We hope that future calculations within the PHSD model [42] might provide azimuthal correlations that will be closer to the measured data. At present the questions noted above regarding the experimental observations have no simple explanation.

V. SUMMARY AND OUTLOOK

We have extended the hadron string dynamics model to describe the formation of the retarded electromagnetic field, its evolution during a nuclear collision and the effect of this field on particle propagation. The case of the Au+Au collision at $\sqrt{s_{NN}} = 200$ GeV for $b = 10$ fm is considered in great detail. It is quite important to understand

the interplay of strong and electromagnetic interactions in this case since it provides a point which is decisive in the CME measurements at RHIC as a function of centrality [28, 29]. It is shown that the most intensive magnetic field oriented perpendicularly to the reaction plane is formed during the time when the Lorentz-contracted nuclei are passing through each other, $t \lesssim 0.2$ fm/c. The maximal strength of the magnetic field here attains very high values, $eB_y/m_\pi^2 \sim 5$. This magnetic field strength is higher by about 3-4 orders of magnitude than that at the surface of the magnetar [49] which in turn is only slightly above the field strength in the star core [50]. Still larger magnetic fields up to $B \sim 10^{24}$ G might have appeared in the early universe [51]. It is impossible to make steady fields stronger than $4.5 \cdot 10^5$ gauss in the laboratory because the magnetic stresses of such fields exceed the tensile strength of terrestrial materials.

This maximal strength of the magnetic field is created predominantly by spectators. When target and projectile remainders are separated, the spectator contribution goes sharply down and for $t \sim 1$ fm/c decreases by more than three orders of magnitude. In subsequent times the participants come into the game, but their contributions are small due to the mutual compensation of approximately equal number of positive and negative charges as well as to the suppressive role of the relativistic retardation effect.

The general pattern of the magnetic field is highly inhomogeneous. However, in the “almond” transverse area (besides the boundary region) the field distributions in z or time look very similar, which allows us to use some simplifying assumptions in phenomenological CME estimates [26, 27].

The important accompanying quantity is the energy density ε of the created particles. Its space-time distributions have been presented. It was shown that the location of maxima in the field strength eB_y and the energy density ε nicely correlate with each other. Thus, it is a necessary condition for a realization of the CME.

In the early time moments the created electric field is perpendicular to the magnetic one and has a dominant x -component. In contrast to the eB_y distribution, the eE_x distribution in the $(x-z)$ space plane has a minimum in the center of the overlap region due to the “hedgehog” field structure of an isolated electric charge. The maximal strength of the electric field is by a factor about 5 lower than that of the magnetic field. For $t \gtrsim 0.20$ fm/c the electric field is small and can be even neglected.

The electromagnetic field is only moderately (within factor ~ 5) changed with impact parameter and collision energy (for $\sqrt{s_{NN}} \approx 200$ -60 GeV) and strongly suppressed for $t \gtrsim 0.2$ fm/c. The scale of the energy density change is much larger but up to times of a few fm/c $\varepsilon > 1$ GeV/fm³ and thereby does not prevent quark-gluon plasma formation. Certainly, the issue of thermalization remains open in this consideration. The very small influence of the electromagnetic field on observables is due to rather large masses of quasiparticles and the point that

the system spends a very short time in a state with an extremely high electromagnetic field.

The comparison of global observables calculated in the HSD model with and without an electromagnetic field reveals no difference apart from the transverse momentum dependence of the elliptic flow where the model results slightly differ in the range $p_t \sim 1$ GeV/c.

Our analysis of the angular correlators - specific for the CME shows that the calculated HSD background is very small and not able to describe the STAR measurements [28, 29]. The consideration of in-plane and out-of-plane projection components of this correlator does not allow us to clarify the picture and rises new questions related to the experiment [32, 33]. In this respect it is of great interest to include quark-gluon degrees of freedom directly in our approach. In particular, the partonic generalization of the HSD model (PHSD) [42] is highly suited for this aim. Another way to approach the CME is to sim-

ulate an induced chromoelectric field which is assumed to be the source of the observed electric charge separation of pion pairs relative to the reaction plane. Alternative mechanisms of charge azimuthal asymmetry should be also carefully studied. Certainly, measurements of the CME at other bombarding energies as well as a search for new observables are very important.

Acknowledgments

We are thankful to M. Gorenstein, D. Kharzeev, V. Koch, V. Skokov, and H. Warringa for useful discussion and remarks. This work has been supported by the LOEWE Center HIC for FAIR. V.T. is partially supported by a Heisenberg-Landau grant.

[1] K. G. Klimenko, Z. Phys. **C54**, 323 (1992); V. P. Gusynin, V. A. Miransky and I. A. Shovkovy, Phys. Rev. Lett. **73**, 3499 (1994) [Erratum-ibid. **76**, 1005 (1996)]; Phys. Lett. **B349**, 477 (1995); Phys. Rev. **D52**, 4747 (1995); Nucl. Phys. **B463**, 249 (1996); K. G. Klimenko and D. Ebert, Phys. Atom. Nucl. **68**, 124 (2005), Yad. Fiz. **68**, 126 (2005).

[2] K. G. Klimenko and V. C. Zhukovsky, Phys. Lett. **B665**, 352 (2008).

[3] F. Preis, A. Rebhan and A. Schmitt, arXiv:1012.4785.

[4] D. T. Son and A. R. Zhitnitsky, Phys. Rev. **D70**, 074018 (2004); M. A. Metlitski and A. R. Zhitnitsky, Phys. Rev. **D72**, 045011 (2005); E. V. Gorbar, V. A. Miransky and I. A. Shovkovy, Phys. Lett. **B695**, 354 (2011).

[5] D. T. Son and M. A. Stephanov, Phys. Rev. **D77**, 014021 (2008).

[6] I. E. Frolov, V. Ch. Zhukovsky and K. G. Klimenko, Phys. Rev. **D82**, 076002 (2010).

[7] M. G. Alford, J. Berges and K. Rajagopal, Nucl. Phys. **B571**, 269 (2000); E. V. Gorbar, Phys. Rev. **D62**, 014007 (2000); E. J. Ferrer, V. de la Incera and C. Manuel, Nucl. Phys. **B747**, 88 (2006); E. J. Ferrer and V. de la Incera, Phys. Rev. **D76**, 114012 (2007); E. J. Ferrer, V. de la Incera and C. Manuel, Phys. Rev. Lett. **95**, 152002 (2005); E. J. Ferrer and V. de la Incera, Phys. Rev. **D76**, 045011 (2007); K. Fukushima and H. J. Warringa, Phys. Rev. Lett. **100**, 032007 (2008); J. L. Noronha and I. A. Shovkovy, Phys. Rev. **D76**, 105030 (2007); T. Mandal, P. Jaikumar and S. Digal, arXiv: 0912.1413; S. Fayazbakhsh and N. Sadooghi, Phys. Rev. **D82**, 045010 (2010); Phys. Rev. **D 83**, 025026 (2011); N. Callebaut, D. Dудal and H. Verschelde, arXiv:1102.3103.

[8] A. A. Sokolov and I. M. Ternov, *"Synchrotron Radiation"* (Oxford, Pergamon Press), 1968.

[9] A. Studenikin, J. Phys. A: Math. Theor. **41**, 164047 (2008); A. Grigoriev, A. Studenikin and A. Ternov, Phys. Lett. **B622**, 199 (2005); I. Balantsev, Yu. Popov and A. Studenikin, Il Nuovo Cimento **C32**, 53 (2009); I. A. Balantsev, Yu. V. Popov and A. I. Studenikin, arXiv:1012.5592; A. I. Titov, B. Kampfer, H. Takabe and A. Hosaka, Phys. Rev. **D83**, 093008 (20010).

[10] N. O. Agasian and S. M. Fedorov, Phys. Lett. **B663**, 445 (2008).

[11] E. S. Fraga and A. J. Mizher, Phys. Rev. **D78**, 025016 (2008).

[12] J. K. Boomsma and D. Boer, Phys. Rev. **D81**, 074005 (2010).

[13] B. Chatterjee, H. Mishra and A. Mishra, arXiv:1102.0875.

[14] A. J. Mizher, M. N. Chernodub and E. S. Fraga, Phys. Rev. **D82**, 105016 (2010); E. S. Fraga, A. J. Mizher and M. N. Chernodub, PoS (ICHEP) 340.

[15] K. Fukushima, M. Ruggieri and R. Gatto, Phys. Rev. **D81**, 114031 (2010); M. Ruggieri, AIP Conf. Proc. **1317**, 360 (2011).

[16] M. DElia, S. Mukherjee and F. Sanfilippo, Phys. Rev. **D82**, 051501 (2010); P. V. Buividovich, M. N. Chernodub, E. V. Luschevskaya and M. I. Polikarpov, Phys. Lett. **B682**, 484 (2010).

[17] R. Gatto and M. Ruggieri, Phys. Rev. **D82**, 054027 (2010); R. Gatto and M. Ruggieri, Phys. Rev. **D83**, 034016 (2011); Marco Ruggieri, arXiv:1102.1832; A. Gynter, K. Landsteiner, F. Pena-Benitez and A. Rebhan, arXiv:1005.2587; J. Mizher, E. S. Fraga and M. N. Chernodub, arXiv:1103.0954.

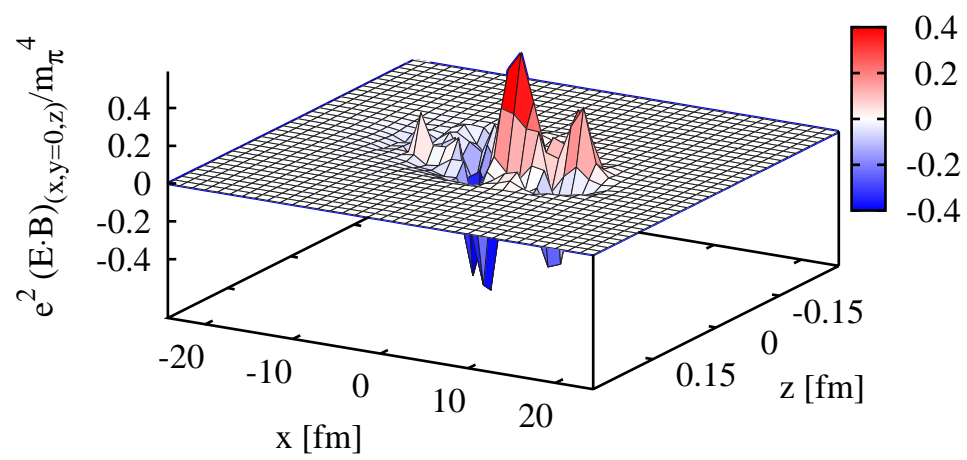
[18] P. Elm fors, K. Enqvist and K. Kainulainen, Phys. Lett. **B440**, 269 (1998); V. Skalozub and M. Bordag, Int. J. Mod. Phys. **A15**, 349 (2000); A. Ayala, A. Bashir, A. Raya and A. Sanchez, Phys. Rev. **D80**, 036005 (2009); J. Navarro, A. Sanchez, M. E. Tejeda-Yeomans, A. Ayala and G. Piccinelli, Phys. Rev. **D82**, 123007 (2010); A. Sanchez, A. Ayala and G. Piccinelli, Phys. Rev. **D75**, 043004 (2007); N. Sadooghi and K. Sohrabi Anaraki, Phys. Rev. **D78**, 125019 (2008).

[19] D. Kharzeev, R. D. Pisarski and M. N. G. Tytget, Phys. Rev. Lett. **81**, 512 (1998); D. Kharzeev and R. D. Pisarski, Phys. Rev. **D61**, 111901 (2000); D. Kharzeev, Phys. Lett. **B633** (2006) 260.

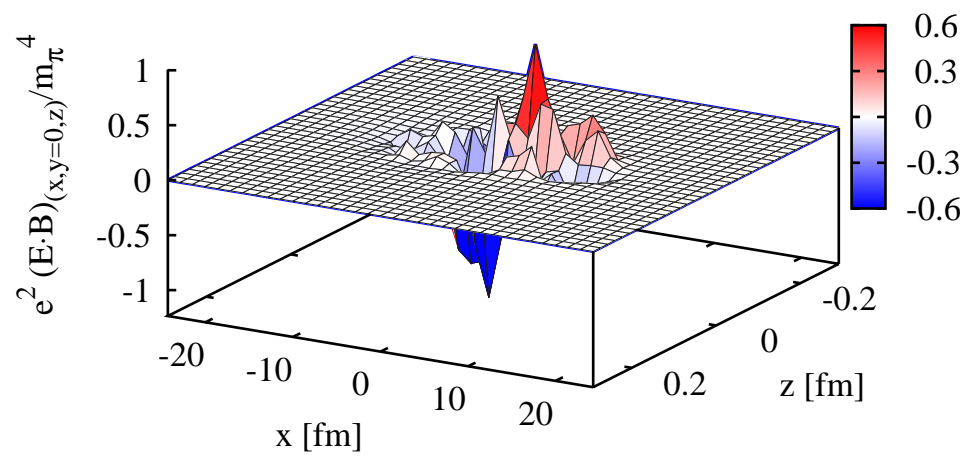
[20] D. Kharzeev and A. Zhitnicky, Nucl. Phys. **A797**, 67 (2007).

- [21] D. E. Kharzeev, L. D. McLerran and H. J. Warringa, Nucl. Phys. **A803**, 227 (2008).
- [22] K. Fukushima, D. E. Kharzeev and H. J. Warringa, Phys. Rev. **D78**, 074033 (2008).
- [23] D. E. Kharzeev and H. J. Warringa, Phys. Rev. **D80**, 034028 (2009).
- [24] P. V. Buiividovich, M. N. Chernodub, E. V. Luschevskaya and M. I. Polikarpov, Phys. Rev. **D80**, 0540503 (2009); Phys. Rev. **D81**, 036007 (2010).
- [25] M. Abramczyk, T. Blum, G. Petropoulos and R. Zhou, PoS LAT2009, 181 (2009).
- [26] V. Skokov, A. Illarionov and V. Toneev, Int. J. Mod. Phys. A **24**, 5925 (2009).
- [27] V. Toneev and V. Voronyuk, Talk at the workshop "Hot and Cold Baryonic Matter", Budapest, August 15-19, 2010, arXiv:1011.5589.
- [28] S. Voloshin for the STAR Collaboration, Nucl. Phys. **A830**, 377c (2009); The STAR Collaboration: B. I. Abelev, et al., Phys. Rev. Lett. **103**, 251601 (2009).
- [29] STAR Collaboration: B. I. Abelev, et al., Phys. Rev. **C81**, 054908 (2010).
- [30] F. Wang, Phys. Rev. **C81**, 064902 (2010).
- [31] S. Pratt, arXiv:1002.1758; S. Schlichting and S. Pratt, arXiv:1005.5341.
- [32] A. Bzdak, V. Koch and J. Liao, Phys. Rev. **C81**, 031901 (2010); arXiv:0912.5050.
- [33] A. Bzdak, V. Koch and J. Liao, Phys. Rev. **C83**, 014905 (2011).
- [34] M. Asakawa, A. Majumder and B. Müller, Phys. Rev. **C81**, 064912 (2010).
- [35] R. Millo and E. Shuryak, arXiv:0912.4894.
- [36] W. Ehehalt and W. Cassing, Nucl. Phys. **A602**, 449 (1996); W. Cassing and E.L. Bratkovskaya, Phys. Rep. **308**, 65 (1999).
- [37] W. Cassing and S. Juchem, Nucl. Phys. **A665**, 377 (2000).
- [38] W. Cassing and S. Juchem, Nucl. Phys. **A672**, 417 (2000).
- [39] W. Cassing and S. Juchem, Nucl. Phys. **A677**, 445 (2000).
- [40] Yu. B. Ivanov, Nucl. Phys. **A474**, 669 (1987).
- [41] D. N. Voskresensky and N. Y. Anisimov, Sov. Phys. JETP **51**, 13 (1980) [Zh. Eksp. Teor. Fiz. **78**, 28 (1980)].
- [42] W. Cassing and E. L. Bratkovskaya, Phys. Rev. **C78**, 034919 (2008); W. Cassing, E. Phys. J. ST **168**, 3 (2009); W. Cassing and E.L. Bratkovskaya, Nucl. Phys. **A831**, 215 (2009); E. L. Bratkovskaya, W. Cassing, V.P. Konchakovski and O. Linnyk, arXiv:1101.5793 (Nucl. Phys A, in press).
- [43] E. Shuryak, Nucl.Phys. **A715**, 289 (2003).
- [44] P. F. Kolb and U. Heinz, in 'Quark Gluon Plasma 3', Editors: R.C. Hwa and X.-N. Wang, World Scientific, Singapore.
- [45] B. Muller and A. Schafer, Phys. Rev. **C82**, 057902 (2010).
- [46] S. A. Voloshin, Phys. Rev. **C70**, 057901 (2004).
- [47] E. L. Bratkovskaya, W. Cassing, and H. Stöcker, Phys. Rev. **C67** (2003) 054905; E.L. Bratkovskaya et al., Phys. Rev. **C 69**, 054907 (2004); O. Linnyk, E. L. Bratkovskaya, and W. Cassing, Int. J. Mod. Phys. **E17**, 1367 (2008); V. P. Konchakovski, M. I. Gorenstein, E. L. Bratkovskaya, and W. Greiner, J. Phys. **G37**, 073101 (2010); E. L. Bratkovskaya and W. Cassing, Nucl. Phys. **A807**, 214 (2008); E. L. Bratkovskaya, W. Cassing and O. Linnyk, Phys. Lett. **B670**, 428 (2009).
- [48] G.-L. Ma and B. Zhang, arXiv:1101.1701.
- [49] <http://solomon.as.utexas.edu/~duncan/magnetar.html> .
- [50] R. C. Duncan and Ch. Thompson, Astrophys. J. **392**, L9 (1992); Astrophys. J. **408**, 194 (1993).
- [51] D. Grasso and H. R. Rubinstein, Phys. Rept. **348** 163 (2001).
- [52] For brevity, below we shall suppress Ψ in Eq.(22) but the azimuthal angle ϕ should be measured with respect to the reaction plane.

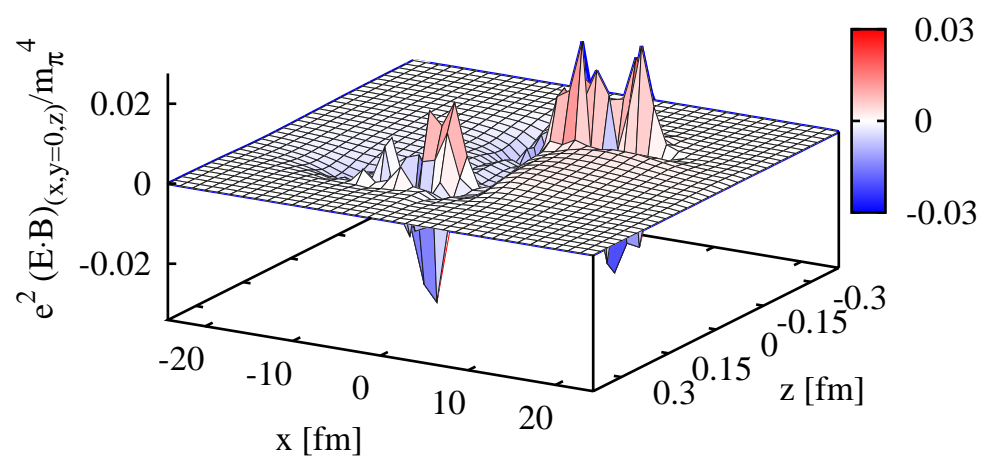
AuAu, $\sqrt{S_{NN}} = 200$ GeV, $b=10$ fm, $t=0.01$ fm/c



AuAu, $\sqrt{S_{NN}} = 200$ GeV, $b=10$ fm, $t=0.05$ fm/c



AuAu, $\sqrt{S_{NN}} = 200$ GeV, $b=10$ fm, $t=0.2$ fm/c



AuAu, $\sqrt{S_{NN}} = 200$ GeV, $b=10$ fm, $t=0.5$ fm/c

